ACS APPLIED MATERIALS & INTERFACES

www.acsami.org

Research Article

Touchless Sensing Interface Based on the Magneto-Piezoresistive Effect of Magnetic Microstructures with Stacked Conductive Coating

Weiguan Zhang, Qinhua Guo, Yu Duan, Qunhui Xu, Chao Shang, Ning Li, and Zhengchun Peng*

Cite This: https://doi.org/10.1021/acsami.1c19137

Read Online

ACCESS | Metrics & More | Article Recommendations | Supporting Information

ABSTRACT: Robotics capable of human-like operations need to have electronic skin (e-skin) with not only tactile sensing functions but also proximity perception abilities. Especially, under the current widespread of COVID-19 pandemic, touchless interfaces are highly desirable. Magneto-reception, with inherent specificity for magnetic objects, is an effective approach to construct a non-contact sensing e-skin. In this work, we propose a new touchless sensing mechanism based on the magneto-piezoresistive effect. The substrate of the sensor is made of hierarchically microstructured ferromagnetic polydimethylsiloxane, coated with a three-dimensional (3D) piezoresistive network. The 3D network is constructed by stacked layers of reduced graphene oxide and carbon nanotubes through layer-by-layer deposition. With this integrated design, a magnetic force induced on the ferromagnetic substrate can seamlessly be applied to the piezoresistive layer of the sensor. Because the magnetic force relates strongly to the approaching distance, the position information can be transduced into the resistance change of the piezoresistive network. The flexible proximity sensor exhibits an ultrahigh spatial resolution of 60 μm, a sensitivity of 50.47 cm^{-1}, a wide working range of 6 cm, and a fast response of 10 ms. The repeatable performance of the sensor is shown by over 5000 cycles of approaching−separation test. We also demonstrate successful application of the sensor in 3D positioning and motion tracking settings, which is critical for touchless tactile perception-based human−machine interactions.

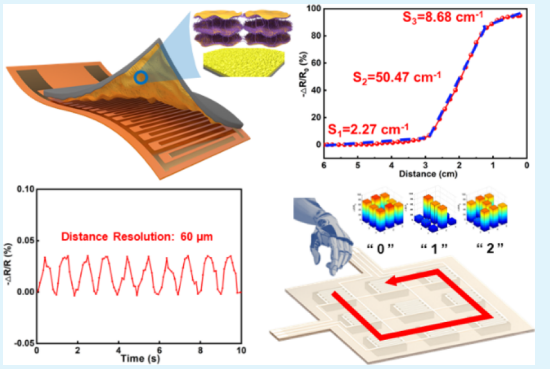

KEYWORDS: *proximity sensing, magneto-piezoresistive effect, stacked piezoresistive network, 3D motion tracking, touchless tactile perception*

1. INTRODUCTION

Electronic skin (e-skin) has achieved rapid development, owing to the excellent flexibility and mechanical compliancy, which can be conformally attached on irregular shapes of robotics or prosthetics for artificial intelligence, health monitoring, and human−machine interactions. Real sensations of human skin like normal and shear force,[1−6] strain,[7−11] temperature, and so forth have all been realized on the e-skin to enrich the sensing capabilities of smart robotics.[12−16] Besides tactile perception, detecting objects away from the e-skin of a robot is also important. For instance, certain tasks require robots to collaborate with human beings. In general, the body parts of a human are very dynamic and may move randomly. It is of great importance to avoid unnecessary collision of a robot with human body parts. A robot equipped with a proximity sensor can detect the distance away from and the moving direction of a human, allowing for timely adjustment of its moving route when needed. This way, the robot can work with human beings with smooth operation and natural interaction. A machine vision system can recognize approaching objects. However, the quality of visual information is affected by many factors, including the light condition, transparency of the objects, and background, that interfere with the moving objects. As such, e-skin with proximity sensing ability is highly demanded.[17,18]

Various mechanisms have been proposed for touchless flexible sensor design including thermal radiation,[19] humidity,[20−23] optical,[24] electrostatic,[18,25] and magnetic.[26−28] Thermal radiation and humidity methods are mainly used for detection of approaching human body parts, like fingers, but have limited working distance due to the rapid attenuation of thermal radiation and moisture; optical methods have superior resolution on distance change but require complex setups and integration that restricts its broad application. Benefiting from easy fabrication and low power consumption, most reported flexible proximity sensors employ a capacitive sensing mechanism with parallel-plate or planar capacitor config-

Received: October 4, 2021
Accepted: December 5, 2021

urations.[29−34] Objects that are conductive or have dielectric constants different from air can cause a change in capacitance when approaching the electrode, owing to the electrostatic coupling effect.[35] However, fundamental challenges for this sensing principle are susceptibility to ubiquitous irrelevant objects and environmental conditions (humidity, air flow, etc.) that make it difficult to distinguish the desired signal source from noises, especially under tiny distance variation.[26,34,35] Also, sensitivity of capacitive-type proximity sensors is largely affected by the limited dielectric between the electrode and objects, which is air in most practical situations. Increasing the density of capacitor arrays is a way of improving sensitivity, but it causes significant mutual capacitance coupling and signal interference between the highly dense intersected capacitors.[34,36]

Magnetic effects have also been widely studied for position detection and navigation applications, owing to their high sensitivity and reliability.[37−41] More importantly, the magnetic field has less disturbance from an ambient environment and is impervious to non-magnetic objects that can ensure accurate acquisition of proximity signals. Until now, the giant magnetoresistive effect has attracted great research interest in making flexible magnetic/proximity sensors, owing to its ultra-high sensitivity and thin-film fabrication technique.[38,40,42−44] However, the precise multilayer deposition of nanometer-thick ferromagnetic and non-magnetic conductive materials involves much higher difficulty and cost in the yield of sensors. The electromagnetic induction mechanism has also been proposed for the detection of an approaching magnetic object, owing to its rapid response.[45−47] However, to achieve adequate induced potential, dense planar coils at the centimeter scale level are required while the most effective sensing area is limited to the center of the coils; besides, such a mechanism is only applicable for dynamic movement monitoring and excludes static location identification. Thus, it is highly demanded to develop a high-performance proximity sensor with a highly adaptable fabrication process and capability for both static and dynamic detecting applications.

In this work, we present a novel flexible proximity sensor based on the magneto-piezoresistive effect for touchless tactile perception including 3D position and motion tracking and human−machine interactions. The sensor is based on ferromagnetic polydimethylsiloxane (PDMS) substrates and stacked piezoresistive layers. The attractive magnetic force induced from the approaching magnetic material will first exert on the ferromagnetic substrate and then transmits to the coated piezoresistive layer that results in the resistance change. As the magnetic force is a function of approaching distance, such resistance change can accurately reflect the proximity of the magnetic objects. The sensing mechanism proposed in this work not only simplifies the fabrication process but also avoids the inferences from the background, thus allowing the proximity sensor with high specificity and accuracy in touchless tactile perception.

To achieve high sensitivity of the sensor, hierarchical magnetic microstructures were constructed by doping Fe_3O_4 nanoparticles in a ferromagnetic PDMS substrate with a two-step sandpaper demolding process. In addition, piezoresistive layers coated on the microstructured ferromagnetic PDMS (MFP) substrate were constructed in a three-dimensional (3D) stacked network for achieving large sensing distance and high spatial resolution of the sensor. The piezoresistive 3D network is fabricated through layer-by-layer deposition of graphene oxide (GO) sheets and carbon nanotubes (CNTs). Then, a thermal reduction is performed to convert the insulating GO to conducting reduced GO (rGO). This annealing process also helps to shape a 3D stacked structure by wrinkling and expanding rGO layers with thermal stress. In addition, it connects CNTs with rGOs both in-plane and out-of-plane, which prepares them for the tunneling effect and contact resistance changing under the influence of magnetic force. With these optimized designs, the sensor offers an ultrahigh sensitivity of 50.47 cm^{-1} and an ultrafast response time of 10 ms with a sensing range up to 6 cm. Because of the ultrahigh sensitivity and low disturbance of magnetic field, a spatial resolution of 60 μm was realized. In addition, no significant degradation of sensing response was observed up to 5000 cycles of approaching−separation test. The magneto-piezoresistive proximity sensor can be used as a touchless sensing interface for human−machine interactions.

2. EXPERIMENTAL SECTION

2.1. Materials. PDMS (Sylgard 184) was purchased from Dow Corning, America. GO powders were purchased from Tulin Jinhua Keji Co., Ltd., Shenzhen, China. Carboxylated single-wall CNTs were purchased from XianFeng Nanao Co. Nanjing, China. Ferroferric oxide nanoparticle (Fe_3O_4; 200 nm) powders were purchased from Shanghai Macklin Biochemical Co., Ltd., Shanghai, China.

2.2. Preparation of the GO and CNT Aqueous Solution. A 2 mg/mL GO aqueous solution was prepared by ultrasonically dispersing 100 mg of GO powders in 50 mL of deionized water in an ultrasonic cleaner under the power of 150 W for 30 min. Addition of 2 mg of CNTs to 20 mL of deionized water, followed by dispersion in a cell crusher for 2 h under 54 W power resulted in a 0.1 mg/mL CNT aqueous solution.

2.3. Preparation of the MFP Substrate. To exactly replicate the microprotrusive morphology of sandpaper, a master mold was first made by casting a PDMS mixture (10:1 weight ratio of the base solution and curing agent) on the sandpaper and heating on a hotplate at 80 °C for 5 h. After being fully cured, the PDMS master mold was obtained by peeling it off from the sandpaper. Then, ferro-PDMS was prepared by adding 50% weighted Fe_3O_4 nanoparticles in the as-prepared PDMS mixture. The ferro-PDMS mixture was fully stirred for 15 min to have the nanoparticles uniformly distributed in PDMS and placed in a vacuum chamber for 10 min to degas. Afterward, the well-prepared ferro-PDMS was cast on the PDMS master mold and cured at 80 °C for 5 h. Finally, the MFP substrate was replicated from the PDMS master mold. Compared to a sandpaper mold, which is easy to break after repeated heating and peeling processes, this master mold is durable and consistent in batch fabrication of the MFP substrates. For easy peeling off, both the sandpaper and PDMS master mold were coated with an anti-sticking monolayer of trichloro (1*H*,1*H*,2*H*,2*H*-perfluorooctyl) silane (FOTS) (Sigma-Aldrich) through thermal evaporation. In this study, we set the thickness of the MFP substrate of the magneto-piezoresistive sensor to be about 1 mm, which not only ensures sufficient magnetic force to be induced but also offers the flexibility needed to attach the sensor on the curved surface of a robot.

2.4. Fabrication of the Magnetic Proximity Sensor. The 3D stacked piezoresistive layer was made by depositing 20 μL of GO and 50 μL of CNT aqueous solutions layer-by-layer on the MFP substrate, which was cut into 1 × 1 cm^2 square pieces. GO and CNT aqueous solutions were prepared by ultrasonically dispersing powders in the deionized water, and their concentrations were 2 and 0.1 mg/mL, respectively. Before each deposition, oxygen plasma treatment was performed on the substrate at 50 W power and 0.4 mbar pressure level for 40 s to improve the hydrophilicity of the surface. Then, the sample was placed in a fume hood for about 1 h to accelerate the natural drying and then cautiously transferred on a hot plate for thermal annealing at 250 °C for 3.5 h under nitrogen. The annealed sample was then facedown mounted on an interdigital electrode

https://doi.org/10.1021/acsami.1c19137
ACS Appl. Mater. Interfaces XXXX, XXX, XXX−XXX

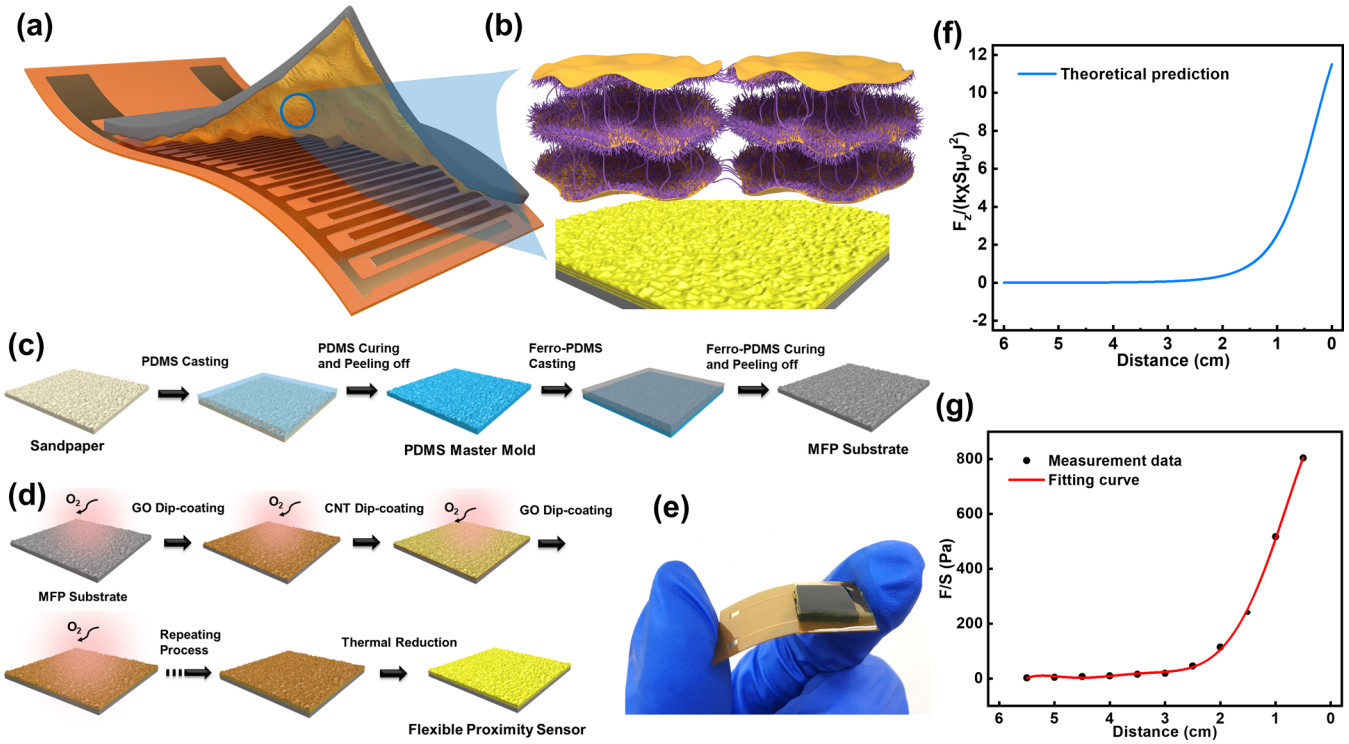

Figure 1. (a) Schematic illustration of the magneto-piezoresistive proximity sensor. (b) Enlarged view of the 3D stacked piezoresistive network coated on the MFP substrate. (c,d) Fabrication process of the MFP substrate and the 3D stacked piezoresistive network through layer-by-layer deposition. (e) Optical image of the fabricated flexible proximity sensor. (f,g) Theoretical prediction and experimental measurement of magnetic force as a function of approaching distance.

fabricated using a flexible printed broad circuit and gently packaged with polyimide adhesive tapes. After all these fabrication steps, the flexible magneto-piezoresistive proximity sensor was completed.

2.5. Characterization of the Sensor. Performance of the proximity sensor was characterized using a dynamic fatigue testing system (ElectroPuls 1000, Instron). Here, the sensor was placed on the bottom stage of the system, while the magnet was fixed in a customized acrylic flat holder clamped using the upper gripper of the system. Diameter of the magnet was 3 cm, which was much larger than the dimension of the sensor to decrease the influence of the fringe effect. After calibration, the approach and separation distance can be controlled by the movement of the gripper, and the real-time resistance change of the sensor was recorded using a digital multimeter (Keithley 6500). Current−voltage (I−V) curves of the sensor at different CNT densities were measured with a source meter (Keithley 2400). The magnetic field under different approaching distances was measured with a digital gauss meter (CH-magneto-electricity 1500), and the magnetic force was characterized using a dynamic fatigue testing system. Surface roughness of the MFP substrate was captured and analyzed using an optical microscope (Leica DM6B) integrated with a 3D imaging analysis system. Morphology observation, element analysis, and mapping of the sensor were all performed using a field-emission scanning electron microscope (Hitachi SU8010).

3. RESULTS AND DISCUSSION

Figure 1a illustrates the schematic drawing of the flexible magnetic proximity sensor. A wrinkled piezoresistive layer was coated on the MFP surface, and the electrical signal would be readout from the interdigital electrodes underneath. Composed of rGO sheets and CNTs, the enlarged morphology of the 3D stacked piezoresistive network is given in Figure 1b. The rGO layers became wrinkled and expanded and were separated horizontally and vertically after the thermal reduction process;[48] also, in the process, with the removal of oxygen-containing functional groups, the sandwiched CNTs bonded to rGO stably and connected them from both in-plane and out-of-plane. The detailed fabrication process of the magneto-piezoresistive proximity sensor is provided in Figure 1c,d. In this work, sandpaper is used to facilitate the formation of hierarchical microstructures on the flexible substrate. As shown in Figure 1c, a PDMS master mold was first made by direct demolding from the sandpaper, and then, ferro-PDMS which was prepared by adding Fe_3O_4 nanoparticles into the PDMS mixture was cast on the master mold. After curing and demolding, microprotrusive structures of sandpaper were precisely reproduced on the ferro-PDMS, and the MPF substrate was fabricated. Then, as shown in Figure 1d, the piezoresistive layer was made by layer-by-layer deposition, in which the dispersed GO and CNT solutions were dip-coated on the MFP surface in a sequential order. Oxygen plasma treatment was carried out before each deposition to increase the hydrophilicity of the surface so that solutions were easily spread out evenly. After natural drying of the solutions, thermal annealing was performed and the flexible proximity sensor with a 3D piezoresistive network on the MFP substrate was obtained. The fabrication process is of high standard and allows good repeatability of the sensor for each manufacturing. Figure 1e shows the optical image of the sensor carefully packaged on a flexible interdigital electrode for signal reading.

The spatially distributed magnetic field plays an important role in transducing distance information into resistance variation through magnetic force. The MFP substrate will be immediately magnetized under the field and pressured by the attractive magnetic force induced by an approaching magnetic material (e.g., permanent magnet). To find out the relationship

https://doi.org/10.1021/acsami.1c19137
ACS Appl. Mater. Interfaces XXXX, XXX, XXX−XXX

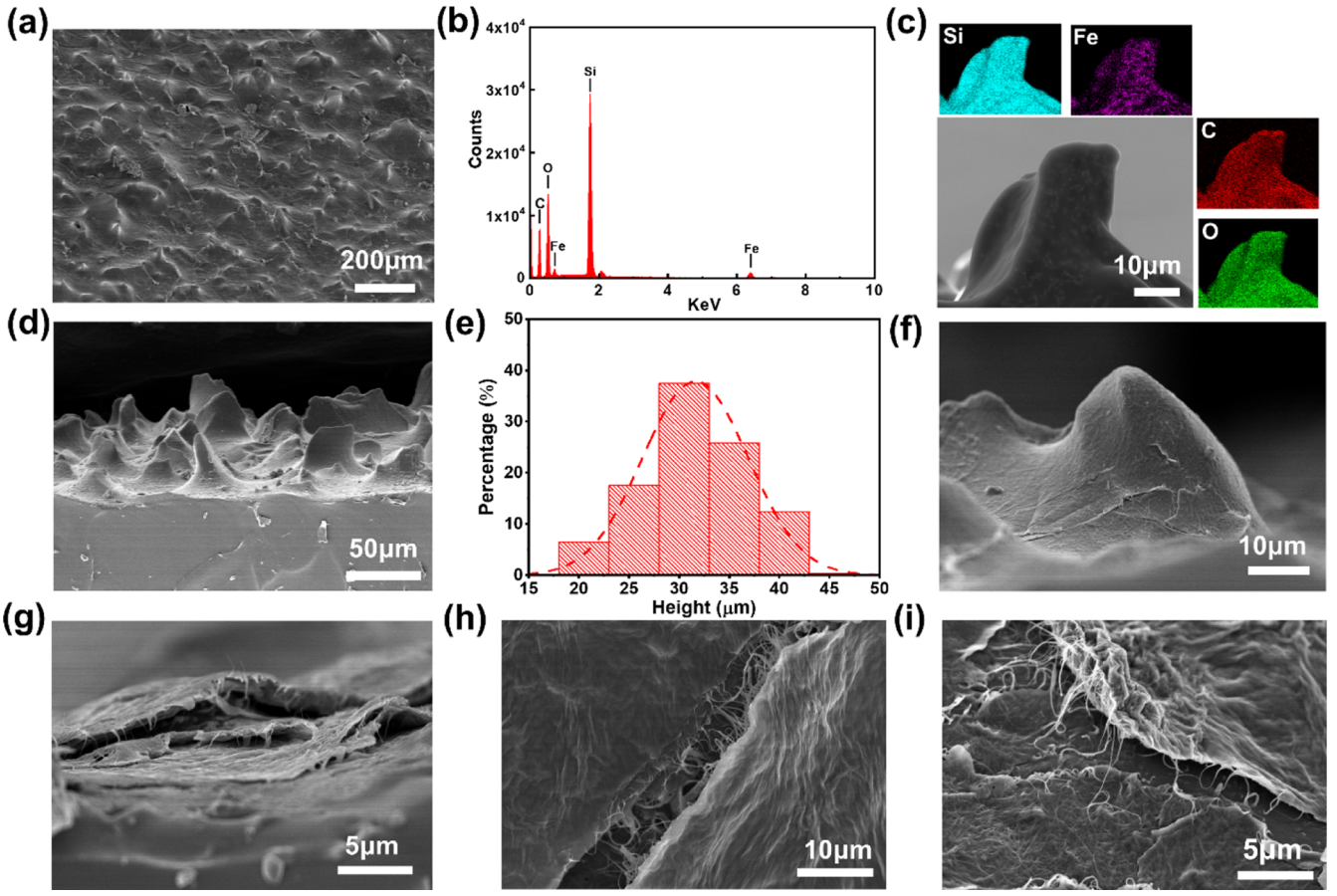

Figure 2. (a) Titled SEM image of the surface topography of the proximity sensor. (b,c) EDS analysis and elemental mapping images of the microprotrusion on the MFP substrate. (d) Cross-sectional SEM image and (e) height distribution analysis of the MFP substrate demolded from #800 sandpaper. (f) Enlarged SEM image of microprotrusion coated with the 3D stacked piezoresistive network. (g–i) SEM image of the 3D piezoresistive network stacked with rGO and CNTs.

between the magnetic force and the approaching distance and the influence of other parameters, an analytical model is derived with the Ampere molecular current hypothesis and Bio-Savart law.[49−51] To simplify the derivation, the Fe_3O_4 nanoparticles are assumed to be uniformly distributed in the PDMS substrate and uniformly magnetized. The normal component of the magnetic force can be expressed as below

$$F_Z(d) = \frac{k\mu_0\chi S J^2}{8}\{[\varphi(H+h+d) - \varphi(H+d)]^2 - [\varphi(H+d) - \varphi(d)]^2\} \quad (1)$$

where k is a self-defined parameter relating to the doping ratio of Fe_3O_4 nanoparticles in the PDMS substrate, μ_0 is the magnetic permeability of vacuum, χ is the magnetic susceptibility of Fe_3O_4 nanoparticles, S is the cross-sectional area of the MFP substrate which is facing the cylindrical permanent magnet, J denotes the current density of the equivalent surface current loop, h is the thickness of permanent magnet, H is the thickness of MFP, and d is their gap distance. In the above expression, the function $\varphi(x)$ is expressed as

$$\varphi(x)\frac{1}{\sqrt{1+\left(\frac{a}{x}\right)^2}} \quad (2)$$

where a is the radius of the permanent magnet. The detailed derivation process is given in section 1 of the Supporting Information. According to eqs 1 and 2, the normalized magnetic force changing with approaching distance is plotted in Figure 1f; meanwhile, the force and magnetic field were also experimentally measured, and the result is shown in Figure 1g and Figure S1 of the Supporting Information. Our analytical model was verified by comparing Figure 1f,g, in which the changing trend of magnetic force with approaching distance is consistent between theoretical prediction and measurement results. Also, it is noted in Figure 1g that the force is smaller at a large distance and increases rapidly with the decrease of the distance.

Figure 2a shows the titled SEM image of the surface topography of the proximity sensor. The ferromagnetic microstructures replicated from #800 sandpaper located randomly on the surface and functioned as mechanical receptors that transmit the induced magnetic force to the piezoresistive layer. Thus, magnetization of these microstructures which is largely determined from the doping condition of Fe_3O_4 nanoparticles is critical for the force transition. Energy-dispersive X-ray spectroscopy (EDS) analysis on the microprotrusion was performed, and the result in Figure 2b shows that the Fe_3O_4 nanoparticles have been successfully mixed into these micro-level structures. Next, the corresponding EDS mapping plotted in Figure 2c demonstrates the uniform distribution of these ferromagnetic particles. Apart from microprotrusions, the flat and cross-sectional areas of the MFP substrate also contain Fe_3O_4

https://doi.org/10.1021/acsami.1c19137
ACS Appl. Mater. Interfaces XXXX, XXX, XXX−XXX

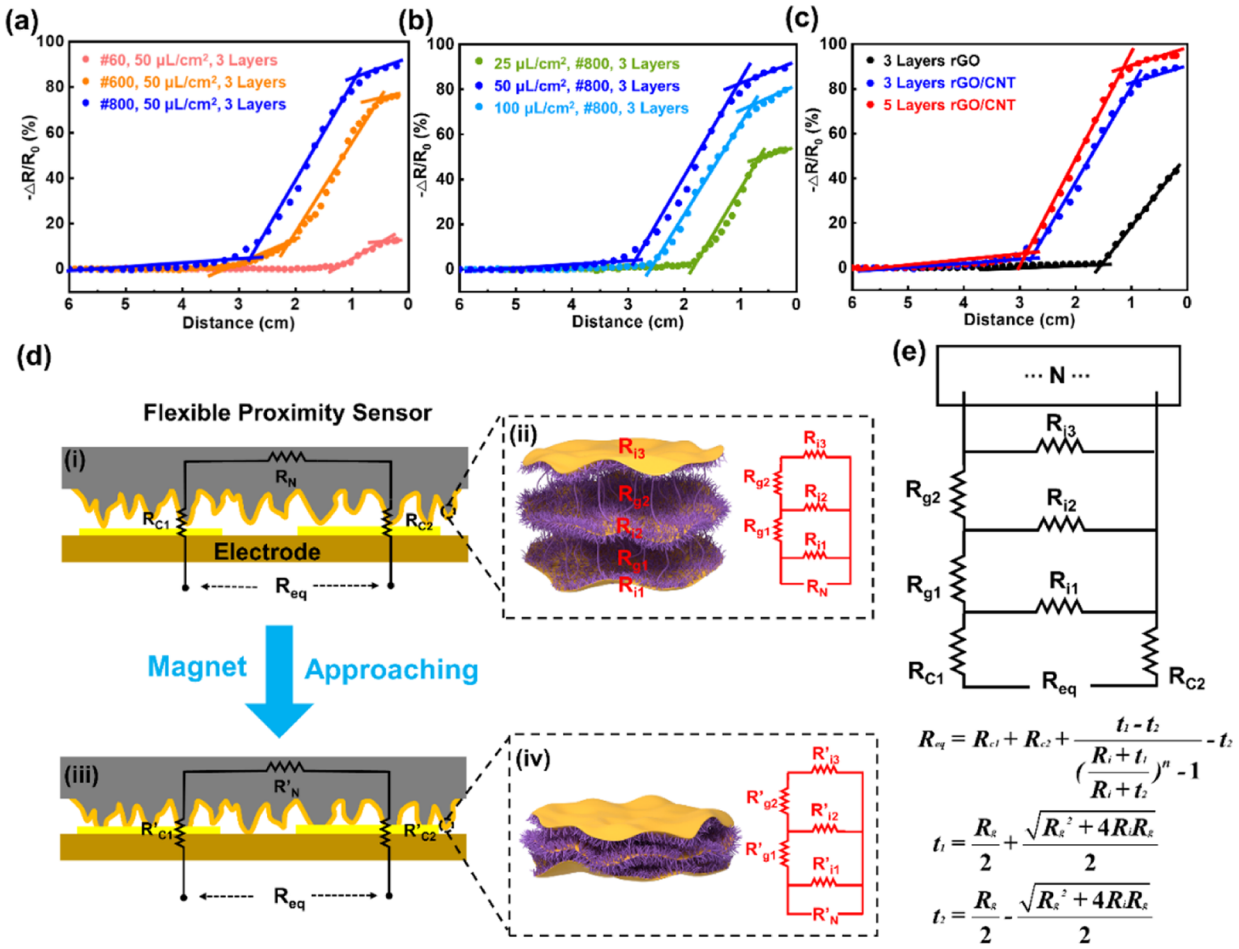

$$R_{eq} = R_{c1} + R_{c2} + \frac{t_1 - t_2}{\left(\frac{R_s + t_1}{R_s + t_2}\right)^n - 1} - t_2$$

$$t_1 = \frac{R_s}{2} + \frac{\sqrt{R_s^2 + 4R_sR_s}}{2}$$

$$t_2 = \frac{R_s}{2} - \frac{\sqrt{R_s^2 + 4R_sR_s}}{2}$$

Figure 3. (a–c) Relative resistance change of the magneto-piezoresistive proximity sensor fabricated with (a) different grid-number sandpapers, (b) different amount of CNTs, and (c) different number of stacked piezoresistive layers. (d) Schematic illustration of the working principle of the proximity sensor. (e) Equivalent circuit model of the proximity sensor.

nanoparticles as proved by the EDS analysis in Figure S2a–c. The SEM image of the cross-sectional view of the MFP substrate in Figure S2d shows that the Fe_3O_4 nanoparticles have no obvious agglomeration. From the cross-sectional SEM image of the sensor in Figure 2d, the microprotrusive structures demolded from #800 sandpaper exhibited a hierarchical morphology, which has been widely proven to be beneficial for sensitivity improvement.[52,53] The height profile of these microstructures was characterized by using an optical microscope equipped with a 3D image analysis system. In Figure 2e, the height distribution of these microprotrusions is analyzed, indicating that around 30 μm-high microprotrusions occupied the largest ratio. Also, these microprotrusions ranged from ~17 to 43 μm high, and such height allows conformal attachment of the 3D piezoresistive network as shown in Figure 2f. The wrinkled rGO sheets overlapped with each other with CNTs being embedded in. The enlarged SEM image of the 3D piezoresistive network is shown in Figure 2g. From the cross-sectional view, the rGO and CNT layers were stacked together with compressible gaps and CNTs functioned as hinges that combined rGO from both in-plane and out-of-plane as demonstrated in Figure 2h,i, respectively.

Design parameters, like MFP substrate roughness, CNT density, and stacked layer numbers of the 3D piezoresistive network, will largely determine the proximity sensor's performance and thus were systematically investigated in this work. MFP substrate roughness which can be engineered using different grid numbers of sandpapers was first studied. Figure 3a compares the relative resistance change of the sensors as a function of the approaching distance from 6 to 0 cm, which were fabricated from #60, #600, and #800 sandpaper. The grid number of sandpapers represents the pore size used for filtering sand grains when making the sandpaper, and a larger number means a smaller pore size and smoother surface.[54] Morphology and height profile analysis of the MFP substrate demolded from #60, #600, and #800 sandpapers are compared in Figure S3 of the Supporting Information, and the microstructures fabricated from #800 sandpaper were the densest and smoothest among the three. According to the response curve in Figure 3a, sensitivity of the magneto-piezoresistive proximity sensor is defined as $S = (\Delta R/R_0)/\Delta d$, where ΔR is the resistance change, R_0 is the initial resistance, and Δd is the change in the approaching distance. Therefore, the maximum sensitivity of the sensor increased from 12.7 to 38.1 to 43.9 cm^{-1} with the decrease in the MFP substrate roughness, and #800 sandpaper obtained the highest sensitivity in this work. It is because denser and lower microprotrusions mean smaller height difference, and thus, more contact sites for electronic paths between microstructures and electrode can be built atthe same magnetic force level that leads to larger resistance variation under small approaching distance change. The data in Figure 3a show that the sensitivity of the magneto-

https://doi.org/10.1021/acsami.1c19137
ACS Appl. Mater. Interfaces XXXX, XXX, XXX–XXX

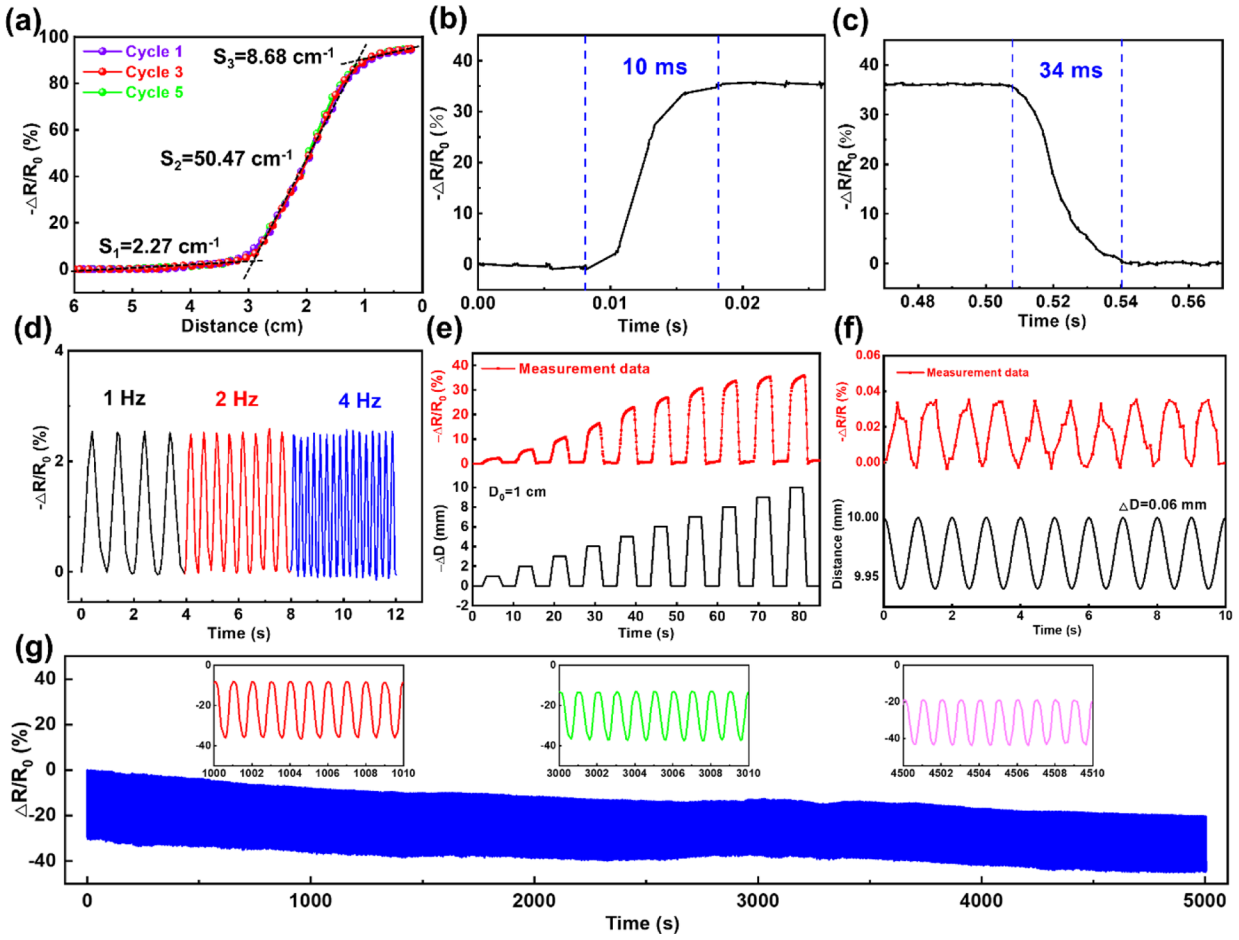

Figure 4. (a) Cyclic test of the magneto-piezoresistive sensor in the entire working distance. (b,c) Response and recovery times of the sensor. (d) Response of the sensor at 1, 2, and 4 Hz approaching−separation frequencies. (e) Dynamic response of the sensor under a 1 mm step-by-step approach from 1 cm separation distance to 0 cm. (f) Response of the sensor to sinusoidal oscillation of the magnet with 60 μm amplitude at 1 cm distance away. (g) Sensor under repeated approaching−separation tests for 5000 cycles at 1 cm distance away (insets are responses at the beginning, middle, and end of the test).

piezoresistive sensor as a function of the approaching distance has three segments. This phenomenon can be explained by the compressing process of the 3D microstructures. Large approaching distance induces small magnetic force, so it is difficult to compress the microstructures to establish more contact sites with electrodes. With little change in the contact area, the change in resistance is small, leading to low sensitivity. As the approaching distance is reduced, the increase in magnetic force compresses more microstructures into contact with the electrode, resulting in large change in resistance and high sensitivity. Although continuously decreasing the distance leads to continual increase in the magnetic force (Figure 1g), the already compressed 3D microstructures leave little room for further increase in the contact area, so the sensitivity of the sensor drops dramatically.

As the outermost layer of the sensor, the 3D stacked piezoresistive network coated on the MFP substrate will perceive the external stimuli in the first place and thus determines the maximum sensing distance of the sensor. In the 3D network, CNTs not only combine rGO sheets from both in-plane and out-of-plane but also behave as the ultra-sensitive conductive paths after connecting with each other. Thus, density of CNTs which is defined by dipping volume divided by the coating area (V/A) was investigated under the influence of sensing distance. With a sensor area of 1 × 1 cm^2, the density was varied from 25 to 50 and 100 μL/cm^2, and response of the sensors was characterized. From Figure 3b, the maximum sensing distance of 6 cm was achieved with 50 μL/cm^2 CNT density, and the sensing distance decreased to 2.5 and 2 cm when CNT density of 100 and 25 μL/cm^2 was used, respectively. Such results were attributed to the combined contact resistant effect and tunneling effect of CNTs in the formation of conductive paths under the influence of the magnetic force. In the stacked structure of the 3D network as illustrated in Figure 2g−i, CNTs were generally classified into two statuses, partially contacted with rGO layers or interacted with each other and others were randomly and individually outspreaded without any connection. When the density was 25 μL/cm^2, CNTs were distributed incompactly so that the potential conductive paths induced by CNTs were less. Thus, the magnetic object needs to be present at a maximum of 2 cm away from the sensor in order for the sensor to generate detectable signals. Increasing the density of CNTs to 50 μL/cm^2 not only causes sufficient change in the contact resistance under compression but also significantly increases the tunneling effect that leads to resistance change before contact.[55] This guarantees that the sensor can respond to both a tiny magnetic force when the magnetic object is far away and a small change in the approaching distance. As the density of CNTs reached 100 μL/cm^2, plenty of CNTs filled in

https://doi.org/10.1021/acsami.1c19137
ACS Appl. Mater. Interfaces XXXX, XXX, XXX−XXX

the network where lots of conductive paths already existed and variation from both the contact resistance and tunneling resistance was reduced after compression. As a result, the sensing distances shrunk from 6 to 2.5 cm. An inflection point for optimized CNT density should exist between 25 and 100 μL/cm^2, and in this work, we used 50 μL/cm^2 for further characterization.

The number of layers in constructing the 3D stacked piezoresistive network was also studied. With fixed conditions of the #800 sandpaper MFP substrate and 50 μL/cm^2 CNT density, the magneto-piezoresistive proximity sensor was fabricated with three rGO layers (no CNT layer), three rGO/CNT layers (rGO/CNT/rGO), and five rGO/CNT layers (rGO/CNT/rGO/CNT/rGO) individually, and their response is shown in Figure 3c. It is obvious that the maximum sensitivity of the sensor with only rGO layers was 32.2 cm^{-1}, which is the lowest due to lack of CNTs in the stacked piezoresistive network for forming ultrasensitive conductive paths. On increasing three rGO/CNT layers to five rGO/CNT layers, one more layer of CNTs was constructed such that resistance of the sensor further decreases as compared in Figure S4 of the Supporting Information. Also, the resistance variations from both contact resistance and tunneling resistance of CNTs were amplified during compression of the microprotrusions; thus, sensitivity of the sensor increased from 43.9 to 50.47 cm^{-1}. Theoretically, having more layers of rGO/CNT would lead to better performance; however, considering the time and cost of fabrication and stability of the 3D stacked network, five rGO/CNT layers were adopted for sensor design in this work.

The working principle of the magneto-piezoresistive proximity sensor is schematically illustrated in Figure 3d. The MFP substrate coated with the 3D stacked piezoresistive network is facedown mounted on an interdigital electrode, and the initial electronic paths are from the contact sites between higher microprotrusions and electrodes, and their contact resistances are defined as R_{C1} and R_{C2}; meanwhile, the inherent resistance of the 3D piezoresistive network is R_N, so the equivalent resistance of the sensor R_{eq} is determined from the two parts depicted in Figure 3d(i). Specifically, as illustrated in Figure 3d(ii), R_N is composed of in-plane resistance R_i and gap resistance R_g, where R_g is the combination of contact resistance and tunneling resistance induced by CNTs. The subscript number represents the layer number of the resistance. After applying magnetic force, more contact sites between microprotrusions and electrodes will be built, causing the change in contact resistance R_{C1} and R_{C2}; also, the compressed 3D network leads to a change in R_N. Compare to R_i, R_g contributes more to the resistance variation, which means that both the contact resistance and tunneling resistance decrease significantly when more conductive paths from CNTs are generated, as demonstrated in Figure 3d(iv). Figure 3e shows the equivalent circuit model of the proximity sensor and the equivalent resistance expression according to the working principle discussed above.

Systematic characterization of the optimized proximity sensor was performed. Figure 4a shows the repeated test of the sensor response in the entire working distance. Overlapped data from five cycles of tests imply that the sensor can work accurately and repeatably each time, and the sensitivity is 2.27 cm^{-1} when approaching distance is from 6 to 3 cm and reaches as high as 50.47 cm^{-1} when approaching distance is from 3 to 1 cm and then decreases to 8.68 cm^{-1} when the distance is close to 0 cm. Although the magnetic force increases linearly when the magnet approaches the sensor, the sensitivity of the magneto-piezoresistive sensor drops during the process. This is mainly attributed to the nonlinear piezoresistive response of the sensor as illustrated in Figure S5. Beyond 0.3 kPa, the 3D piezoresistive network is fully compressed, leading to dramatic drop in the sensitivity. From Figure S5, the piezoresistive response range of the magneto-piezoresistive proximity sensor reaches to 10 kPa, which is larger than magnetic force-induced pressure at contact (1 kPa), proving it can also respond to pressure after contacting, which is superior to a regular magnetic-type proximity sensor. Figure S6 of the Supporting Information compares the performance of reported flexible proximity sensors in terms of maximum sensitivity and sensing distance.[17,19,29,31,32,34,56−58] It indicates that our magneto-piezoresistive sensor has the highest sensitivity among all the proximity sensors reported so far. To further improve the sensing distance of our sensor, both the higher doping ratios of Fe_3O_4 nanoparticles and more layers of the 3D piezoresistive network can be employed to produce larger resistance change of the sensor at a given approaching distance. Response time of the sensor was then characterized using a custom-made platform integrated with a non-magnetic plate and ejection mechanism. With the ejection system, a magnet can be instantly placed in space at a given distance from the sensor and then be driven to approach to and separate from the sensor. During this process, a digital multimeter is used to record the real-time resistance change of the magneto-piezoresistive sensor. From the data in Figure 4b,c, the response and recovery time is calculated to be 10 and 34 ms, respectively. With the rapid response time, frequency property of the sensor was characterized. Figure 4d shows sensor response at 1, 2, and 4 Hz approaching−separation frequencies with an initial distance of 1 cm away and an oscillation amplitude of 1 mm. The result demonstrated stable and accurate response of the sensor to corresponding frequencies. Then, a continuous measurement with gradually decreasing approaching distance was performed. From the base distance of 1 cm, a 1 mm step-by-step decrease in approaching distance was employed, and relative resistance variation of the sensor shown in Figure 4e exhibited a linear and stable response correlated to the distance change. To explore the minimal detectable distance change of the sensor, the magnet moved frequently in a sinusoidal wave at 1 Hz. As the change in the distance shrank down to 60 μm, the magneto-piezoresistive sensor can still record a 0.04% variation in the resistance (Figure 4f), indicating that the sensor has a spatial resolution of 60 μm. According to the relationship between the magnetic field and distance (Figure S1), 60 μm resolution corresponds to a magnetic field change of 750 μT. Such a change is 15 times larger than that of the geomagnetic field (~50 μT). Therefore, the influence of geomagnetic field is negligible. To the best of our knowledge, the resolution obtained in this work is the best level among all reported flexible proximity sensors. Figure 4g shows the repeatability of the sensor performance under continuous approach and separation test for over 5000 cycles at 1 Hz. During the test, the resistance of the magneto-piezoresistive sensor became smaller over time, owing to more CNTs staying in contact with each other. This phenomenon gradually caused a slight drift of the baseline. However, the relative change in resistance remains almost the same throughout the repeatability test (insets of Figure 4g), proving the robustness of the sensor for long-term usage.

https://doi.org/10.1021/acsami.1c19137
ACS Appl. Mater. Interfaces XXXX, XXX, XXX−XXX

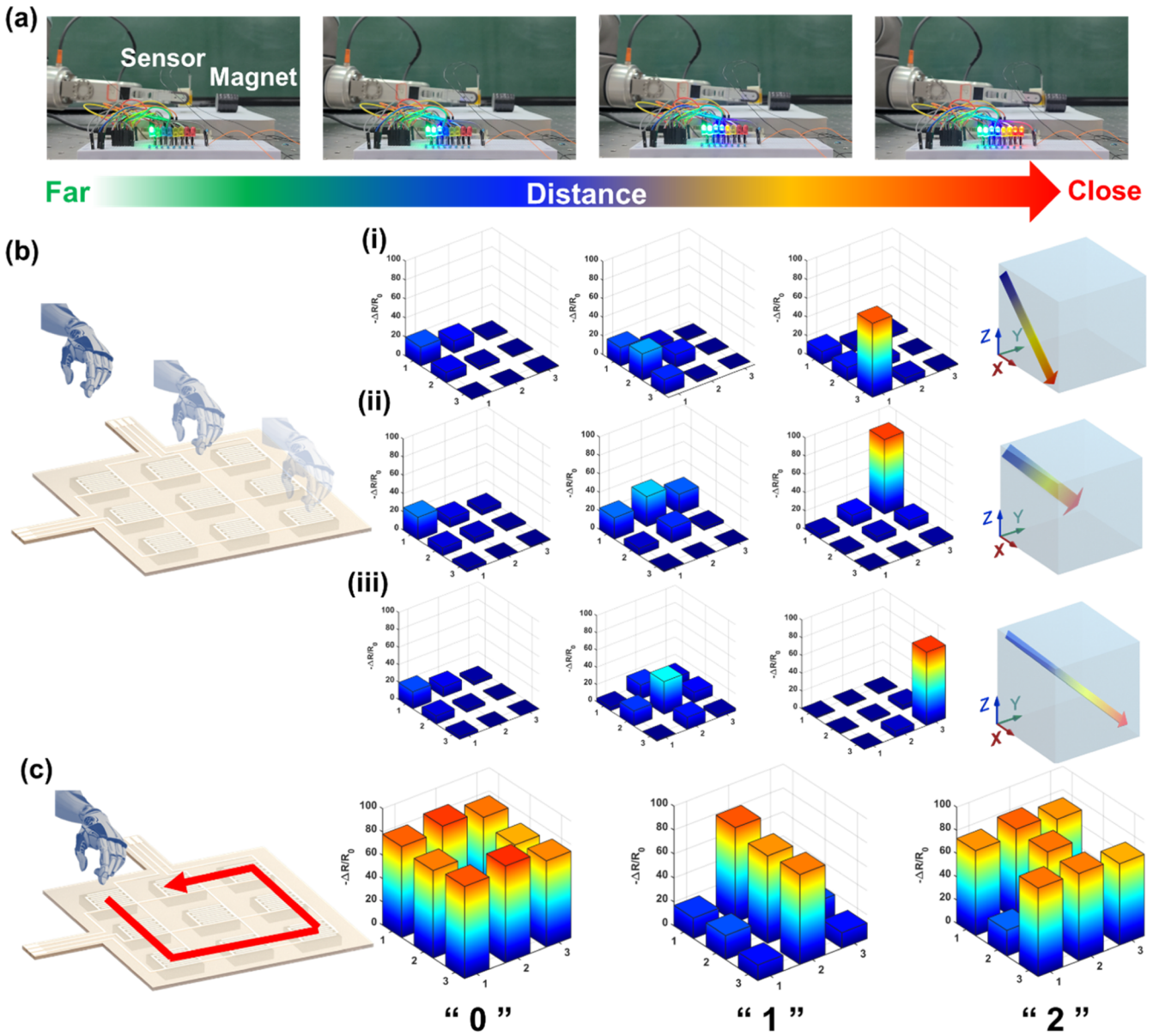

Figure 5. (a) Position of the robotic hand detected by the magneto-piezoresistive sensor and visualized by the lighting color and number of LEDs. (b) 3D motion tracking of the robotic hand moving in *x*, *y*, and diagonal directions by a sensor array. (c) Number identification by the sensor array.

Owing to the series of excellent features mentioned above, the magneto-piezoresistive proximity sensor can be employed for acquiring highly accurate 3D position and motion information, which are critical for the operation of smart robotics. Figure 5a illustrates the position detection of the robotic hand visualized by the lighting color and number of LEDs. The sensor was packaged on the finger of the robotic hand and connected to a self-made control system, which could programmatically regulate the on/off of LEDs on the board. When the robotic hand was 5 cm away from the magnet, one of the eight LEDs was on, and with its approach toward the magnetic material, eight LEDs gradually lightened to reflect the position of the robotic hand. Also, the color change from green to red was used as a reminder for the approaching status (a video for the entire process is included as Movie S1 in the Supporting Information). Besides the 1D position recognition, we made a 3 × 3 sensor array for motion detection of robotics as shown in Figure S7 in the Supporting Information. Compared to the flexible pressure sensor array used for motion detection,[59,60] touchless tactile perception proposed in this work not only provides in-plane moving direction according to sequential response of adjunct sensors but also gives out-of-plane approaching distance information from the single sensor and thus 3D motion tracking of robotics can be realized. In Figure 5b(i)−(iii), the robotic hand with its fingers equipped with magnetic material was driven in *x*, *y*, and the diagonal directions. The trajectories were all successfully recognized by the sensor array. Movie S2 of the Supporting Information demonstrates the successful 3D motion detection using the sensor array. Benefiting from the 3D motion tracking, the sensor array could also function as an interface to identify characters and numbers that smart robotics intend to communicate with other machines or robotics. Figure 5c shows that the writing of numbers “0”, “1”, and “2” using the robotic hand were all distinguished by the sensor array.

https://doi.org/10.1021/acsami.1c19137
ACS Appl. Mater. Interfaces XXXX, XXX, XXX−XXX

Having proved such capabilities in position and 3D motion tracking, our proposed interface can also be applied for touchless human−machine interactions. An important human−machine interaction scenario for touchless operation is in hospital, especially in the COVID-19 pandemic. To avoid the spread of virus and protect both medical staff and patients, touchless interaction has been recommended by centers for disease control and prevention of most countries.[61] Thus, in this work, we developed a touchless human−machine interaction system for checking medical reports for medical staffs. Generally, the system can be installed at the service terminal of hospitals, in which after inputting the patient's identification number, related medical information will be loaded and displayed to medical staff. As shown in Figure 6(i),

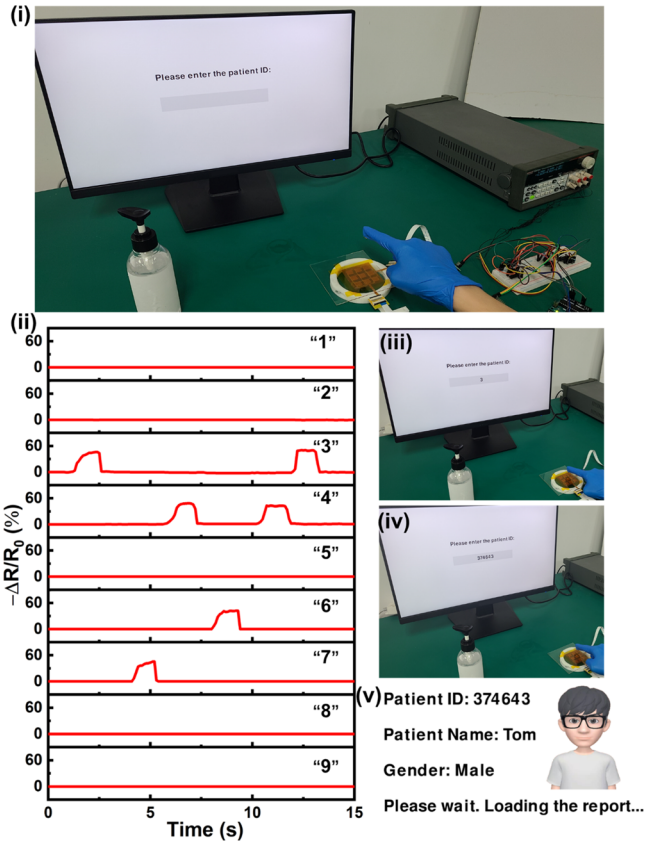

Figure 6. Touchless human−machine interaction system for non-contact medical information checking. (i) Illustration of the touchless interaction system and the user interface. (ii) Signal reading with the magneto-piezoresistive sensor array. (iii−v) Response of the user interface to the input.

the volunteer wore a regular medical glove with magnetic material adhered to the tip area of the index finger and then contactlessly input the patient ID number into the interface. Concerning real practical situations in hospitals, sterilization of gloves with ethyl alcohol is always required; thus, in the demonstration, the volunteer also had his glove wiped with alcohol gel first and then performed the operation. To avoid the interference signals during the transient cross-moving of fingers on non-target numbers, a duration time of 1 s was set to guarantee the correct selection of target numbers. Figure 6(ii) shows the measured time domain response of the sensor array, in which corresponding numbers are all distinguished. Figure 6(iii,iv) shows the number inputting through the interface, showing that environmental influence (wet glove) had no impact on the signal identification, and also, the combined dynamic and static tracking improved the accuracy of signal acquisition, benefiting from the magneto-piezoresistive effect. After successfully entering the patient ID number, related information was displayed on the screen as shown in Figure 6(v). The complete demonstration of the touchless interface is shown in Movie S3 of the Supporting Information. Overall, the touchless interface system proposed in this work can be widely used in non-contact human−machine interaction applications.

4. CONCLUSIONS

In summary, a novel magneto-piezoresistive proximity sensor was developed by having hierarchical MFP coated with a 3D piezoresistive network for touchless tactile perception. Based on the magneto-piezoresistive effect, the approaching distance-related magnetic force is induced on the MFP and then applies to the piezoresistive layer seamlessly so that proximity information can be transduced into resistance change of the sensor. Benefiting from the hierarchical microstructures and stacked piezoresistive layers, the flexible proximity sensor shows an ultrahigh resolution of 60 μm and a sensitivity of 50.47 cm^{-1}; a fast response time of 10 ms, and a wide sensing range of 6 cm are also achieved. Our sensor exhibits more than 500% increase in sensitivity than that of previously reported flexible proximity sensors and almost two orders of magnitude higher resolution than the conventional capacitive proximity sensors. Besides, stable response for over 5000 cycles of approaching-separation test proves the robustness of the sensor. Finally, we demonstrate its application in 3D position recognition and motion tracking, which is highly demanded for safety control and precise operation of robotics. Furthermore, this touchless sensing interface offers an effective way to restrain the COVID-19 virus from spreading widely.

■ ASSOCIATED CONTENT

Supporting Information

The Supporting Information is available free of charge at https://pubs.acs.org/doi/10.1021/acsami.1c19137.

Derivation of the attractive magnetic force; measured magnetic induction induced by the magnet as a function of the approaching distance; EDS analysis and elemental mapping on the top surface of the MFP substrate; elemental mapping on the cross section of the MFP substrate; view of Fe_3O_4 nanoparticles dispersed in PDMS; 3D microscopy images and height profile analysis of the MFP substrate demolded from #60, #600, and #800 sandpapers; measured $I-V$ curve of the magneto-piezoresistive proximity sensor with different layer numbers in constructing the 3D stacked piezoresistive network; measured piezoresistive response of the magneto-piezoresistive sensor; comparison of the sensitivity and sensing distance of flexible proximity sensors based on different sensing mechanisms; and optical image of the flexible magneto-piezoresistive proximity sensor array (PDF)

Position of the robotic hand detected by the magneto-piezoresistive proximity sensor (MP4)

3D motion tracking using a flexible magneto-piezoresistive proximity sensor array (MP4)

Touchless human−machine interaction system (MP4)

https://doi.org/10.1021/acsami.1c19137
ACS Appl. Mater. Interfaces XXXX, XXX, XXX−XXX

AUTHOR INFORMATION

Corresponding Author

Zhengchun Peng − *Center for Stretchable Electronics and Nano Sensors, College of Physics and Optoelectronic Engineering, Shenzhen University, Shenzhen 518060, China;* orcid.org/0000-0002-7114-1797; Email: zcpeng@szu.edu.cn

Authors

Weiguan Zhang − *Center for Stretchable Electronics and Nano Sensors, College of Physics and Optoelectronic Engineering and College of Mechatronics and Control Engineering, Shenzhen University, Shenzhen 518060, China;* orcid.org/0000-0002-3725-4130

Qinhua Guo − *Center for Stretchable Electronics and Nano Sensors, College of Physics and Optoelectronic Engineering, Shenzhen University, Shenzhen 518060, China;* orcid.org/0000-0003-2171-1971

Yu Duan − *Center for Stretchable Electronics and Nano Sensors, College of Physics and Optoelectronic Engineering, Shenzhen University, Shenzhen 518060, China*

Qunhui Xu − *Center for Stretchable Electronics and Nano Sensors, College of Physics and Optoelectronic Engineering, Shenzhen University, Shenzhen 518060, China*

Chao Shang − *Center for Stretchable Electronics and Nano Sensors, College of Physics and Optoelectronic Engineering, Shenzhen University, Shenzhen 518060, China*

Ning Li − *College of Mechatronics and Control Engineering, Shenzhen University, Shenzhen 518060, China*

Complete contact information is available at: https://pubs.acs.org/10.1021/acsami.1c19137

Author Contributions

W.Z. and Q.G. contributed equally to this work. W.Z. proposed the idea and designed the methodology of the work. Q.G. did the data curation, analysis, and investigation of the work. Q.G. and Y.D. fabricated the device. Q.X. and C.S. performed the data visualization of the device for human−machine interfacing. N.L. participated in the discussion for device fabrication. W.Z. and Q.G. wrote the original article. Z.P. complemented the idea, supervised the research, and edited the article.

Notes

The authors declare no competing financial interest.

ACKNOWLEDGMENTS

This work was financially supported by the National Natural Science Foundation of China (61904112) and the Science and Technology Innovation Commission of Shenzhen (KQTD20170810105439418, JCYJ20190808142609414, and JCYJ20180305124942832).

REFERENCES

(1) Yan, Y. C.; Hu, Z.; Yang, Z. B.; Yuan, W. Z.; Song, C. Y.; Pan, J.; Shen, Y. J. Soft Magnetic Skin for Super-Resolution Tactile Sensing with Force Self-Decoupling. *Sci. Rob.* **2021**, *6*, No. eabc8801.

(2) Boutry, C. M.; Negre, M.; Jorda, M.; Vardoulis, O.; Chortos, A.; Khatib, O.; Bao, Z. N. A Hierarchically Patterned, Bioinspired E-Skin able to Detect the Direction of Applied Pressure for Robotics. *Sci. Rob.* **2018**, *3*, No. eaau6914.

(3) Bai, N.; Wang, L.; Wang, Q.; Deng, J.; Wang, Y.; Lu, P.; Huang, J.; Li, G.; Zhang, Y.; Yang, J.; Xie, K.; Zhao, X.; Guo, C. F. Graded Intrafillable Architecture-Based Iontronic Pressure Sensor with Ultra-Broad-Range High Sensitivity. *Nat. Commun.* **2020**, *11*, 209.

(4) He, F.; You, X.; Wang, W.; Bai, T.; Xue, G.; Ye, M. Recent Progress in Flexible Microstructural Pressure Sensors toward Human-Machine Interaction and Healthcare Applications. *Small Methods* **2021**, *5*, 2001041.

(5) Zhang, W.; Xiao, Y.; Duan, Y.; Li, N.; Wu, L.; Lou, Y.; Wang, H.; Peng, Z. A High-Performance Flexible Pressure Sensor Realized by Overhanging Cobweb-like Structure on a Micropost Array. *ACS Appl. Mater. Interfaces* **2020**, *12*, 48938−48947.

(6) Chen, D.; Liu, Z.; Li, Y.; Sun, D.; Liu, X.; Pang, J.; Liu, H.; Zhou, W. Unsymmetrical Alveolate PMMA/MWCNT Film as a Piezoresistive E-Skin with Four-Dimensional Resolution and Application for Detecting Motion Direction and Airflow Rate. *ACS Appl. Mater. Interfaces* **2020**, *12*, 30896−30904.

(7) Wang, C.; Xia, K.; Wang, H.; Liang, X.; Yin, Z.; Zhang, Y. Advanced Carbon for Flexible and Wearable Electronics. *Adv. Mater.* **2019**, *31*, 1801072.

(8) Ge, G.; Lu, Y.; Qu, X.; Zhao, W.; Ren, Y.; Wang, W.; Wang, Q.; Huang, W.; Dong, X. Muscle-Inspired Self-Healing Hydrogels for Strain and Temperature Sensor. *ACS Nano* **2020**, *14*, 218−228.

(9) O'Driscoll, D. P.; McMahon, S.; Garcia, J.; Biccai, S.; Gabbett, C.; Kelly, A. G.; Barwich, S.; Moebius, M.; Boland, C. S.; Coleman, J. N. Printable G-Putty for Frequency- and Rate-Independent, High-Performance Strain Sensors. *Small* **2021**, *17*, 2006542.

(10) Lin, J.; Cai, X.; Liu, Z.; Liu, N.; Xie, M.; Zhou, B.; Wang, H.; Guo, Z. Anti-liquid-Interfering and Bacterially Antiadhesive Strategy for Highly Stretchable and Ultrasensitive Strain Sensors Based on Cassie-Baxter Wetting State. *Adv. Funct. Mater.* **2020**, *30*, 2000398.

(11) Tang, N.; Zhou, C.; Qu, D.; Fang, Y.; Zheng, Y.; Hu, W.; Jin, K.; Wu, W.; Duan, X.; Haick, H. A Highly Aligned Nanowire-Based Strain Sensor for Ultrasensitive Monitoring of Subtle Human Motion. *Small* **2020**, *16*, 2001363.

(12) Yang, Y.; Song, Y.; Bo, X.; Min, J.; Pak, O. S.; Zhu, L.; Wang, M.; Tu, J.; Kogan, A.; Zhang, H.; Hsiai, T. K.; Li, Z.; Gao, W. A Laser-Engraved Wearable Sensor for Sensitive Detection of Uric Acid and Tyrosine in Sweat. *Nat. Biotechnol.* **2020**, *38*, 217.

(13) Shi, X.; Wu, P. A Smart Patch with On-Demand Detachable Adhesion for Bioelectronics. *Small* **2021**, *17*, 2101220.

(14) Yu, Y.; Nassar, J.; Xu, C. H.; Min, J. H.; Yang, Y. R.; Dai, A.; Doshi, R.; Huang, A.; Song, Y.; Gehlhar, R.; Ames, A. D.; Gao, W. Biofuel-Powered Soft Electronic Skin with Multiplexed and Wireless Sensing for Human-Machine Interfaces. *Sci. Rob.* **2020**, *5*, No. eaaz7946.

(15) Xiong, J.; Chen, J.; Lee, P. S. Functional Fibers and Fabrics for Soft Robotics, Wearables, and Human-Robot Interface. *Adv. Mater.* **2021**, *33*, 2002640.

(16) Peng, B.; Zhao, F.; Ping, J.; Ying, Y. Recent Advances in Nanomaterial-Enabled Wearable Sensors: Material Synthesis, Sensor Design, and Personal Health Monitoring. *Small* **2020**, *16*, 2002681.

(17) Lu, L.; Jiang, C.; Hu, G.; Liu, J.; Yang, B. Flexible Noncontact Sensing for Human-Machine Interaction. *Adv. Mater.* **2021**, *33*, 2100218.

(18) Tang, Y.; Zhou, H.; Sun, X.; Diao, N.; Wang, J.; Zhang, B.; Qin, C.; Liang, E.; Mao, Y. Triboelectric Touch-Free Screen Sensor for Noncontact Gesture Recognizing. *Adv. Funct. Mater.* **2020**, *30*, 1907893.

(19) Cao, Z.; Yang, Y.; Zheng, Y.; Wu, W.; Xu, F.; Wang, R.; Sun, J. Highly Flexible and Sensitive Temperature Sensors Based on Ti3C2Tx (MXene) for Electronic Skin. *J. Mater. Chem. A* **2019**, *7*, 25314−25323.

(20) Yang, J.; Shi, R.; Lou, Z.; Chai, R.; Jiang, K.; Shen, G. Flexible Smart Noncontact Control Systems with Ultrasensitive Humidity Sensors. *Small* **2019**, *15*, 1902801.

(21) Li, N.; Jiang, Y.; Zhou, C.; Xiao, Y.; Meng, B.; Wang, Z.; Huang, D.; Xing, C.; Peng, Z. High-Performance Humidity Sensor Based on Urchin-Like Composite of Ti3C2 MXene-Derived TiO2 Nanowires. *ACS Appl. Mater. Interfaces* **2019**, *11*, 38116−38125.

(22) Duan, Z.; Jiang, Y.; Yan, M.; Wang, S.; Yuan, Z.; Zhao, Q.; Sun, P.; Xie, G.; Du, X.; Tai, H. Facile, Flexible, Cost-Saving, and Environment-Friendly Paper-Based Humidity Sensor for Multifunctional Applications. *ACS Appl. Mater. Interfaces* **2019**, *11*, 21840−21849.
(23) Zhou, K.; Xu, W.; Yu, Y.; Zhai, W.; Yuan, Z.; Dai, K.; Zheng, G.; Mi, L.; Pan, C.; Liu, C.; Shen, C. Tunable and Nacre-Mimetic Multifunctional Electronic Skins for Highly Stretchable Contact-Noncontact Sensing. *Small* **2021**, *17*, 2100542.
(24) Oh, N.; Kim, B. H.; Cho, S.-Y.; Nam, S.; Rogers, S. P.; Jiang, Y.; Flanagan, J. C.; Zhai, Y.; Kim, J.-H.; Lee, J.; Yu, Y.; Cho, Y. K.; Hur, G.; Zhang, J.; Trefonas, P.; Rogers, J. A.; Shim, M. Double-Heterojunction Nanorod Light-Responsive LEDs for Display Applications. *Science* **2017**, *355*, 616−619.
(25) Chen, S.; Wang, Y.; Yang, L.; Guo, Y.; Wang, M.; Sun, K. Flexible and Transparent Sensors with Hierarchically Micro-Nano Texture for Touchless Sensing and Controlling. *Nano Energy* **2021**, *82*, 105719.
(26) Ge, J.; Wang, X.; Drack, M.; Volkov, O.; Liang, M.; Cañón Bermúdez, G. S.; Illing, R.; Wang, C.; Zhou, S.; Fassbender, J.; Kaltenbrunner, M.; Makarov, D. A Bimodal Soft Electronic Skin for Tactile and Touchless Interaction in Real Time. *Nat. Commun.* **2019**, *10*, 4405.
(27) Makushko, P.; Oliveros Mata, E. S.; Cañón Bermúdez, G. S.; Hassan, M.; Laureti, S.; Rinaldi, C.; Fagiani, F.; Barucca, G.; Schmidt, N.; Zabila, Y.; Kosub, T.; Illing, R.; Volkov, O.; Vladymyrskyi, I.; Fassbender, J.; Albrecht, M.; Varvaro, G.; Makarov, D. Flexible Magnetoreceptor with Tunable Intrinsic Logic for On-Skin Touchless Human-Machine Interfaces. *Adv. Funct. Mater.* **2021**, *31*, 2101089.
(28) Cañón Bermúdez, G. S.; Fuchs, H.; Bischoff, L.; Fassbender, J.; Makarov, D. Electronic-Skin Compasses for Geomagnetic Field-Driven Artificial Magnetoreception and Interactive Electronics. *Nat. Electron.* **2018**, *1*, 589−595.
(29) Guo, H.; Tan, Y. J.; Chen, G.; Wang, Z.; Susanto, G. J.; See, H. H.; Yang, Z.; Lim, Z. W.; Yang, L.; Tee, B. C. K. Artificially Innervated Self-Healing Foams as Synthetic Piezo-Impedance Sensor Skins. *Nat. Commun.* **2020**, *11*, 5747.
(30) Guan, F.; Xie, Y.; Wu, H.; Meng, Y.; Shi, Y.; Gao, M.; Zhang, Z.; Chen, S.; Chen, Y.; Wang, H.; Pei, Q. Silver Nanowire-Bacterial Cellulose Composite Fiber-Based Sensor for Highly Sensitive Detection of Pressure and Proximity. *ACS Nano* **2020**, *14*, 15428−15439.
(31) Zhang, C.; Liu, S.; Huang, X.; Guo, W.; Li, Y.; Wu, H. A Stretchable Dual-Mode Sensor Array for Multifunctional Robotic Electronic Skin. *Nano Energy* **2019**, *62*, 164−170.
(32) Guo, Y.; Gao, S.; Yue, W.; Zhang, C.; Li, Y. Anodized Aluminum Oxide-Assisted Low-Cost Flexible Capacitive Pressure Sensors Based on Double-Sided Nanopillars by a Facile Fabrication Method. *ACS Appl. Mater. Interfaces* **2019**, *11*, 48594−48603.
(33) Sarwar, M. S.; Dobashi, Y.; Preston, C.; Wyss, J. K.; Mirabbasi, S.; Madden, J. D. Bend, Stretch, and Touch: Locating a Finger on an Actively Deformed Transparent Sensor Array. *Sci. Adv.* **2017**, *3*, No. e1602200.
(34) Zhang, B.; Xiang, Z.; Zhu, S.; Hu, Q.; Cao, Y.; Zhong, J.; Zhong, Q.; Wang, B.; Fang, Y.; Hu, B.; Zhou, J.; Wang, Z. Dual Functional Transparent Film for Proximity and Pressure Sensing. *Nano Res.* **2014**, *7*, 1488−1496.
(35) Ye, Y.; Zhang, C.; He, C.; Wang, X.; Huang, J.; Deng, J. A Review on Applications of Capacitive Displacement Sensing for Capacitive Proximity Sensor. *IEEE Access* **2020**, *8*, 45325−45342.
(36) Kang, M.; Kim, J.; Jang, B.; Chae, Y.; Kim, J.-H.; Ahn, J.-H. Graphene-Based Three-Dimensional Capacitive Touch Sensor for Wearable Electronics. *ACS Nano* **2017**, *11*, 7950−7957.
(37) Melzer, M.; Kaltenbrunner, M.; Makarov, D.; Karnaushenko, D.; Karnaushenko, D.; Sekitani, T.; Someya, T.; Schmidt, O. G. Imperceptible Magnetoelectronics. *Nat. Commun.* **2015**, *6*, 6080.
(38) Kondo, M.; Melzer, M.; Karnaushenko, D.; Uemura, T.; Yoshimoto, S.; Akiyama, M.; Noda, Y.; Araki, T.; Schmidt, O. G.; Sekitani, T. Imperceptible Magnetic Sensor Matrix System Integrated with Organic Driver and Amplifier Circuits. *Sci. Adv.* **2020**, *6*, No. eaay6094.
(39) Franco, F.; Dias, R. A.; Gaspar, J.; de Freitas, S. C.; Freitas, P. P. Hybrid Rigid-Flexible Magnetoresistive Device Based on a Wafer Level Packaging Technology for Micrometric Proximity Measurements. *IEEE Sens. J.* **2019**, *19*, 12363−12368.
(40) Münzenrieder, N.; Karnaushenko, D.; Petti, L.; Cantarella, G.; Vogt, C.; Büthe, L.; Karnaushenko, D. D.; Schmidt, O. G.; Makarov, D.; Tröster, G. Entirely Flexible On-Site Conditioned Magnetic Sensorics. *Adv. Electron. Mater.* **2016**, *2*, 1600188.
(41) Pan, Y.-D.; Yu, L.-R.; Wang, L.; Chen, T.; Wei, X.-Y.; Zhu, R.-G.; Li, J.-W.; Feng, C.; Yu, G.-H. Construction of High-Performance Magnetic Sensor Based on Anisotropic Magnetoresistance Ta/MgO/NiFe/MgO/Ta Film. *Rare Met.* **2021**, *40*, 2026−2032.
(42) Cañón Bermúdez, G. S.; Karnaushenko, D. D.; Karnaushenko, D.; Lebanov, A.; Bischoff, L.; Kaltenbrunner, M.; Fassbender, J.; Schmidt, O. G.; Makarov, D. Magnetosensitive E-Skins with Directional Perception for Augmented Reality. *Sci. Adv.* **2018**, *4*, No. eaao2623.
(43) Cañón Bermúdez, G. S.; Makarov, D. Magnetosensitive E-Skins for Interactive Devices. *Adv. Funct. Mater.* **2021**, *31*, 2007788.
(44) Ha, M.; Cañón Bermúdez, G. S.; Kosub, T.; Mönch, I.; Zabila, Y.; Oliveros Mata, E. S.; Illing, R.; Wang, Y.; Fassbender, J.; Makarov, D. Printable and Stretchable Giant Magnetoresistive Sensors for Highly Compliant and Skin-Conformal Electronics. *Adv. Mater.* **2021**, *33*, 2005521.
(45) Liu, L.; Shi, Q.; Sun, Z.; Lee, C. Magnetic-Interaction Assisted Hybridized Triboelectric-Electromagnetic Nanogenerator for Advanced Human-Machine Interfaces. *Nano Energy* **2021**, *86*, 106154.
(46) Wan, J.; Wang, H.; Miao, L.; Chen, X.; Song, Y.; Guo, H.; Xu, C.; Ren, Z.; Zhang, H. A Flexible Hybridized Electromagnetic-Triboelectric Nanogenerator and Its Application for 3D Trajectory Sensing. *Nano Energy* **2020**, *74*, 104878.
(47) Jiang, D.; Ouyang, H.; Shi, B.; Zou, Y.; Tan, P.; Qu, X.; Chao, S.; Xi, Y.; Zhao, C.; Fan, Y.; Li, Z. A Wearable Noncontact Free-Rotating Hybrid Nanogenerator for Self-Powered Electronics. *InfoMat* **2020**, *2*, 1191−1200.
(48) Liu, W.; Liu, N.; Yue, Y.; Rao, J.; Cheng, F.; Su, J.; Liu, Z.; Gao, Y. Piezoresistive Pressure Sensor Based on Synergistical Innerconnect Polyvinyl Alcohol Nanowires/Wrinkled Graphene Film. *Small* **2018**, *14*, 1704149.
(49) Guo, X.- f.; Yang, Y.; Zheng, X. J. Analytic Expression of Magnetic Field Distribution of Rectangular Permanent Magnets. *Appl. Math. Mech.* **2004**, *25*, 297−306.
(50) Falkowski, K. The Rings with Molecular Current as the Model of the Passive Magnetic Bearing. *J. Vibroengineering* **2012**, *14*, 135−142.
(51) Schenck, J. F. Safety of Strong, Static Magnetic Fields. *J. Magn. Reson. Imaging* **2000**, *12*, 2−19.
(52) Ruth, S. R. A.; Feig, V. R.; Tran, H.; Bao, Z. Microengineering Pressure Sensor Active Layers for Improved Performance. *Adv. Funct. Mater.* **2020**, *30*, 2003491.
(53) Huang, Y.; Fan, X.; Chen, S. C.; Zhao, N. Emerging Technologies of Flexible Pressure Sensors: Materials, Modeling, Devices, and Manufacturing. *Adv. Funct. Mater.* **2019**, *29*, 1808509.
(54) Xiao, Y.; Duan, Y.; Li, N.; Wu, L.; Meng, B.; Tan, F.; Lou, Y.; Wang, H.; Zhang, W.; Peng, Z. Multilayer Double-Sided Microstructured Flexible Iontronic Pressure Sensor with a Record-wide Linear Working Range. *ACS Sens.* **2021**, *6*, 1785−1795.
(55) Yu, Y.; Song, G.; Sun, L. Determinant Role of Tunneling Resistance in Electrical Conductivity of Polymer Composites Reinforced by Well Dispersed Carbon Nanotubes. *J. Appl. Phys.* **2010**, *108*, 084319.
(56) Liu, Y.-Q.; Zhang, J.-R.; Han, D.-D.; Zhang, Y.-L.; Sun, H.-B. Versatile Electronic Skins with Biomimetic Micronanostructures Fabricated Using Natural Reed Leaves as Templates. *ACS Appl. Mater. Interfaces* **2019**, *11*, 38084−38091.

https://doi.org/10.1021/acsami.1c19137
ACS Appl. Mater. Interfaces XXXX, XXX, XXX−XXX

(57) Wang, H.; Tang, Q.; Zhao, X.; Tong, Y.; Liu, Y. Ultrasensitive Flexible Proximity Sensor Based on Organic Crystal for Location Detection. *ACS Appl. Mater. Interfaces* **2018**, *10*, 2785−2792.
(58) Kulkarni, M. R.; John, R. A.; Rajput, M.; Tiwari, N.; Yantara, N.; Nguyen, A. C.; Mathews, N. Transparent Flexible Multifunctional Nanostructured Architectures for Non-optical Readout, Proximity, and Pressure Sensing. *ACS Appl. Mater. Interfaces* **2017**, *9*, 15015−15021.
(59) Jang, J.; Jun, Y. S.; Seo, H.; Kim, M.; Park, J.-U. Motion Detection Using Tactile Sensors Based on Pressure-Sensitive Transistor Arrays. *Sensors* **2020**, *20*, 3624.
(60) Yang, J. C.; Mun, J.; Kwon, S. Y.; Park, S.; Bao, Z.; Park, S. Electronic Skin: Recent Progress and Future Prospects for Skin-Attachable Devices for Health Monitoring, Robotics, and Prosthetics. *Adv. Mater.* **2019**, *31*, 1904765.
(61) Lee, S. M.; Lee, D. Opportunities and Challenges for Contactless Healthcare Services in the Post-COVID-19 Era. *Technol. Forecast. Soc. Change* **2021**, *167*, 120712.

https://doi.org/10.1021/acsami.1c19137
ACS Appl. Mater. Interfaces XXXX, XXX, XXX−XXX